APPLIED SCIENCES AND ENGINEERING

Electro-plasmonic nanoantenna: A nonfluorescent optical probe for ultrasensitive label-free detection of electrophysiological signals

Ahsan Habib[1], Xiangchao Zhu[1], Uryan I. Can[2], Maverick L. McLanahan[3], Pinar Zorlutuna[2,4,5], Ahmet A. Yanik[1]*

Harnessing the unprecedented spatiotemporal resolution capability of light to detect electrophysiological signals has been the goal of scientists for nearly 50 years. Yet, progress toward that goal remains elusive due to lack of electro-optic translators that can efficiently convert electrical activity to high photon count optical signals. Here, we introduce an ultrasensitive and extremely bright nanoscale electric-field probe overcoming the low photon count limitations of existing optical field reporters. Our electro-plasmonic nanoantennas with drastically enhanced cross sections (~10^4 nm^2 compared to typical values of ~10^{-2} nm^2 for voltage-sensitive fluorescence dyes and ~1 nm^2 for quantum dots) offer reliable detection of local electric-field dynamics with remarkably high sensitivities and signal–to–shot noise ratios (~60 to 220) from diffraction-limited spots. In our electro-optics experiments, we demonstrate high-temporal resolution electric-field measurements at kilohertz frequencies and achieved label-free optical recording of network-level electrogenic activity of cardiomyocyte cells with low-intensity light (11 mW/mm^2).

INTRODUCTION

Electrophysiological activity of cells is of fundamental importance to neuroscience, cardiology, and cellular biology. In this sense, development of techniques optically mapping the electrogenic signals has created substantial interest within the scientific community (*1*–*3*). Photons are remarkably efficient reporters; light offers exceptional spatiotemporal resolution, unparalleled multiplexing, and high-bandwidth operation capabilities well beyond limits of electronic technologies. Harvesting photons for electrophysiological studies, on the other hand, largely depends on our ability to recruit efficient reporters converting local electrogenic activity to high photon count far-field signals (*4*–*7*). Typically, fluorescence molecules that can translate membrane potentials to an optical signal are used (*1*, *3*). These genetically encoded voltage indicators (GEVIs) have fundamental shortcomings associated to bleaching of fluorescent molecules (photostability) and generation of disruptive oxygen free radicals (phototoxicity) (*1*, *4*). Furthermore, GEVIs with tiny cross sections (~10^{-2} nm^2) (*8*) and low quantum yields (~10^{-3} to 10^{-2}) (*2*) offer limited number of fluorescent photons for detection and hence suffer from signal–to–shot noise ratio (SSNR) limitations (*1*, *4*, *5*). More recently, there has been a concerted effort focused on the development of nonfluorescent extracellular optical reporters exploiting inherent voltage sensitivity of noble metals (*9*–*13*). Unlike fluorescence molecules, plasmonic resonators do not have photostability and phototoxicity limitations or require invasive genetic modifications. In principle, plasmonic nanoresonators with exceptionally large cross sections (~10^4 nm^2) offer orders of magnitude enhanced photon-flux measurements from diffraction-limited volumes (*14*). The main weakness of the field voltage reporters, on the other hand, is their low inherent electric-field sensitivity. Electro-optic effects in metals associated to non-Faradaic (electric double layer) charging/discharging are very weak because of extremely high electron densities (*15*, *16*). As a result, optical field measurements using plasmonic nanostructures are readily dominated by shot noise (*16*). Despite extensive efforts, development of label-free and noninvasive optical probes that can detect local electric-field dynamics with high sensitivity, reliability, and spatiotemporal resolution remains elusive.

Here, we introduce a new class of extremely bright label-free optical field probes overcoming the photon count and field sensitivity limitations of state-of-the-art electro-optic field reporters. Our noninvasive extracellular electro-plasmonic nanoprobes, offering more than three orders of magnitude enhanced field sensitivities over conventional plasmonic nanoantennas (*13*), enable high signal-to-noise ratio measurements from diffraction-limited volumes at kilohertz frequencies. To achieve ultrasensitive and high signal-to-noise ratio measurements, we use active lumped nanocircuit elements that are analogous to tunable radio frequency (RF) antennas. Alù and Engheta (*17*–*19*) theoretically formulated that antenna loading, a concept adapted from RF communications, could be used to markedly alter the far-field response of nanoscale plasmonic antennas operating in the optical domain. Subsequent experimental studies have successfully shown tunable nanoantenna response by modifying the optical nanoload using lithographic techniques (*20*, *21*), oxidation-reduction chemistry (*22*), and chemical absorption (*23*, *24*). Here, we introduce biocompatible electrochromic polymer poly(3,4-ethylenedioxythiophene):polystyrene sulfonate (PEDOT:PSS) as an electric field–controlled load enabling active and reversible tuning of the plasmonic resonances (*25*). In reverse operation mode, we show that an electrochromically loaded plasmonic (electro-plasmonic) nanoantenna functions as a reporter of the local electric-field dynamics and electrophysiological activity to the far field. In the following, by projecting the (Au) electrode-PEDOT:PSS system to an equivalent circuit and using electrochemical impedance spectroscopy (EIS) and potential step voltammetry (PSV) measurements, we first optimize the electrochromic load parameters that govern the temporal response of our field probes. Our experiments show that electrochromic switching times of the PEDOT:PSS load can be drastically

[1]School of Engineering, University of California Santa Cruz, Santa Cruz, CA 95064, USA. [2]Aerospace and Mechanical Engineering, University of Notre Dame, Notre Dame, IN 46556, USA. [3]Physics Department, University of California Santa Cruz, Santa Cruz, CA 95064, USA. [4]Chemical and Biomolecular Engineering, University of Notre Dame, Notre Dame, IN 46655, USA. [5]Bioengineering Graduate Program, University of Notre Dame, Notre Dame, IN 46655, USA.
*Corresponding author. Email: yanik@ucsc.edu

improved with lateral and vertical downscaling to nanoscale dimensions. We then introduce a selective electropolymerization technique that enables us to conformally coat a metallic nanoantenna with ultrathin (10 to 20 nm thick) and nanoscale (0.01 μm^2) PEDOT:PSS loads. By performing electro-optic measurements from diffraction-limited volumes, we subsequently demonstrate drastically (~3.25×10^3 times) enhanced field sensitivities with electrochromic loading and establish high SSNR (~60 to 220) measurement capability from single electro-plasmonic nanoprobes. Using dark-field optoelectrochemical measurements, we then prove the high-frequency operation capability of our nanoprobes at kilohertz frequencies with submillisecond (<0.2 ms) temporal response times. Last, through our in vitro experiments, we establish label-free and noninvasive optical measurement of electrogenic activity of human-induced pluripotent stem cell (hiPSC)–derived cardiomyocytes (iCMs) using low-intensity light (11 mW/mm^2), which is two to three orders of magnitude lower than the typical light intensities used for fluorescent voltage probes (*4*). Our nanoprobes, exploiting a novel electro-optic mechanism, put forward a blueprint of an entirely new family of extracellular optical probes with high spatiotemporal resolution and signal-to-noise ratio electrophysiological measurement capability with light. In addition to in vitro uses shown here, in vivo applications of our nanoprobes with infrared light are discussed.

RESULTS

Electro-plasmonic nanoantenna

We use far-field response of the electro-plasmonic nanoantenna to monitor the local electric-field dynamics as summarized in Fig. 1. The scanning electron microscope (SEM) image in Fig. 1A demonstrates the substantial size difference between typical electrogenic (cardiomyocyte) cells and our electro-plasmonic field probes. The key advantage of electro-plasmonic probes is their potential for massive multiplexing through remote transduction of the local electric fields without being restricted by electrode layout or physical connections. An electro-plasmonic nanoantenna (height, 45 nm; diameter, 90 nm), when arrayed with submicrometer periodicity, offers electric-field measurements with light from diffraction-limited spots. Using nanolithographic techniques, an array of 2.25 million electro-plasmonic nanoantennas (500 nm periodicity) is fabricated on a transparent indium tin oxide (ITO)–coated glass substrate. To probe electric-field dynamics, we load the pristine plasmonic nanoantennas with PEDOT:PSS electrochromic polymer (fig. S1 and Materials and Methods). With electrochromic polymers, thicker films are desirable to achieve strong electro-optic signals. Ultrathin layers, on the other hand, are required for faster charge modulation characteristics (*26*). Our analysis based on three-dimensional finite difference time domain (FDTD) simulations shows that the plasmonic nanoantenna strongly confines the electromagnetic field within a narrow region around it (Fig. 1, B and C, and figs. S2). By taking advantage of drastically enhanced light-matter interactions in these plasmonic hotspots, we can simultaneously achieve strong electro-optic sensitivity and fast electrochemical response using ultrathin electrochromic loads.

Adopting RF antenna concepts, the far-field response of our electro-plasmonic nanoantenna to the local electric-field dynamics could be understood within the framework of optical circuit theory (*17*, *27*). Here, the electrochromic load is incorporated to the lumped equivalent nanocircuit as a parallel arm composed of resistive (ohmic losses) and capacitive lumped circuit elements (Fig. 1D). The electric field–controlled capacitance of the electrochromic load couples the low-frequency local electric-field dynamics (<1 kHz) to high-frequency (~460 THz) electromagnetic resonances. In our analysis, we first find the equivalent optical circuit parameters of pristine nanoantenna and then incorporate electrochromic load to it. Optical circuit parameters are obtained using FDTD simulations and a semianalytical retrieval method (text S1; Fig. 1, D and E; and fig. S3) (*21*). Wavelength-dependent susceptances of the lumped nanocircuit elements corresponding to pristine nanoantenna and its electrochromic load are shown in Fig. 1E. Optical circuit resonances occur when the intrinsic susceptance $\mathrm{Im}[1/Z_{antenna}]$ of the pristine nanoantenna (black solid curve) is compensated by the capacitive susceptance $-\omega C_{PEDOT}$ of the electrochromic load in the doped (red curve) and dedoped (blue curve) states. The resonances occur at the intersections highlighted by the circles in Fig. 1E, leading to maximum scattering signal. For the doped (dedoped) electrochromic load, the resonance condition occurs at the shorter (longer)-wavelength intersection (Fig. 1E). This is associated to the diminished resistive losses of the electrochromic load at the corresponding operating wavelength (fig. S2). Our circuit model shows that switching from the doped (red curve) to dedoped (blue curve) state of the electrochromic load causes red shifting of the far-field plasmonic response in agreement with our FDTD simulations (Fig. 1E). Strong agreement in between FDTD simulation and optical circuit models is also observed for the spectral features and quality factors. Far-field response of our electro-plasmonic nanoantenna, a reporter of the local electric-field dynamics, can be measured using spectroscopic or intensity-based techniques.

Nanoscale electrochromic loading for submillisecond response times

To achieve high field sensitivity, we used PEDOT:PSS polymer as a field-controlled nanoload coupled to the metallic nanoantenna (Fig. 2A). In addition to its strong electro-optic properties, PEDOT has a number of advantages: (i) It shows fast and reversible electrochromic response, (ii) it is stable as a thin film (down to 10 nm thicknesses) with high capacitance (routinely used in supercapacitors), (iii) it is a biocompatible polymer that is extensively used in microelectrode arrays to improve electrical coupling between the electrodes and excitable cells, and (iv) it could be functionalized with biomolecules that stimulate cell growth and molecular attachment (*28*, *29*). In our experiments, we doped PEDOT:polymer with poly(styrenesulfonate) (PEDOT:PSS) to lower the electrical impedance to achieve stronger electrical coupling to the local field (*30*). Precisely controlled PEDOT:PSS layers are electropolymerized on gold electrodes using a galvanostatic approach in an aqueous solution containing 10 mM EDOT (3,4-ethylenedioxythiophene) monomer and 0.1 M sodium poly(styrenesulfonate) (NaPSS) (Materials and Methods and fig. S4). Electron microscopy measurements are used to determine the thicknesses of the electrodeposited ultrathin PEDOT:PSS films. Cyclic voltammetry (CV) measurements are subsequently performed to verify the reliability and repeatability of the polymer layer deposition process. Our analysis shows that thicker PEDOT:PSS films yield larger capacitances as shown in Fig. 2B, where the area enclosed by the voltammogram trace is a measure of the total capacitance.

Fast electro-plasmonic response to electric-field dynamics is essential to accurately detect the electrophysiological activity of excitable cells. To optimize the temporal response of our electro-plasmonic nanoantenna, we first evaluated the electrochemical characteristics of the (Au) electrode-PEDOT:PSS system. To determine the RC time

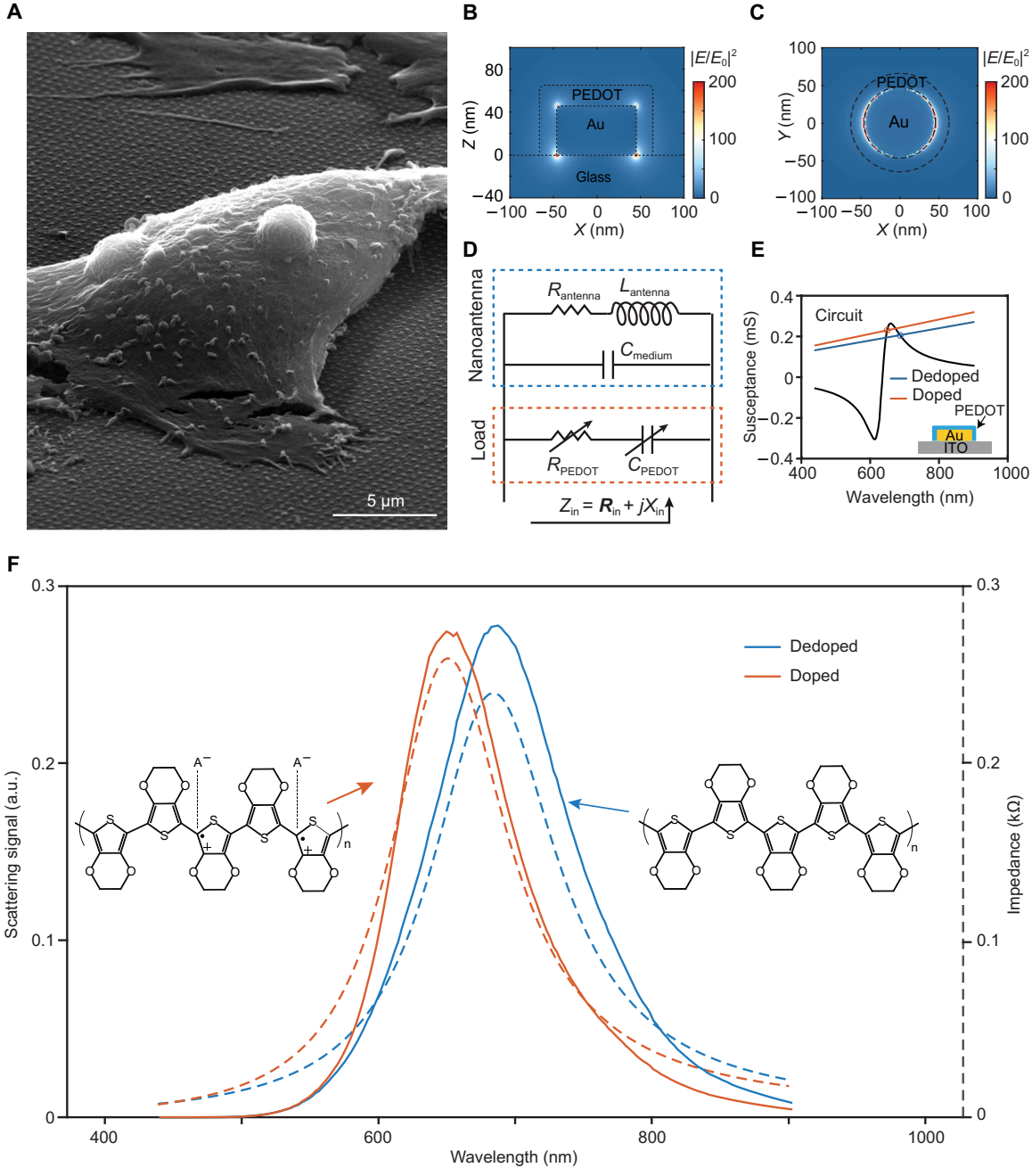

Fig. 1. Electro-plasmonic nanoantenna. (**A**) SEM image of cardiomyocyte cells cultured on an array of electro-plasmonic nanoantennas. Considerable size difference between loaded nanoantennas (height, 45 nm; diameter, 90 nm) and electrogenic cells is shown. A total of 2.25 million electro-plasmonic nanoantennas are incorporated on a transparent substrate with nanometer spatial resolution, allowing measurement of electric-field dynamics from diffraction-limited spots over a large surface area. (**B**) Side view of near-field enhancement $|E/E_0|^2$ along the pristine nanoantenna at 678.8 nm. FDTD simulations show that plasmonic excitations lead to strong confinement of the light within the 20-nm-thick electrochromic layer. (**C**) Top view of the near-field enhancement $|E/E_0|^2$ profile along the center of the pristine nanoantenna at 678.8 nm. (**D**) Equivalent nanocircuit model of the electro-plasmonic nanoantenna. Electrochromic doping is incorporated through tunable resistor and capacitor elements. (**E**) Susceptances of the gold nanoantenna and the PEDOT:PSS load for doped (red) and dedoped states (blue) are shown. Intersections (indicated by the circles) correspond to the open-circuit condition, the plasmonic resonance. For the doped (dedoped) electrochromic load, the resonance condition occurs at the shorter (longer) wavelength intersection due to the diminished resistance (losses) of the electrochromic load. (**F**) Far-field response of the electro-plasmonic nanoantenna to the doping state of electrochromic load. Electrochromic switching of the load from the doped (red curve) to the dedoped (blue curve) state leads to red shifting of the plasmonic resonance. FDTD stimulations (solid curves) and lumped nanocircuit model (dashed curves) are compared. The inset depicts the chemical structure of PEDOT for the doped (left) and dedoped (right) state. A^- represents the counterions.

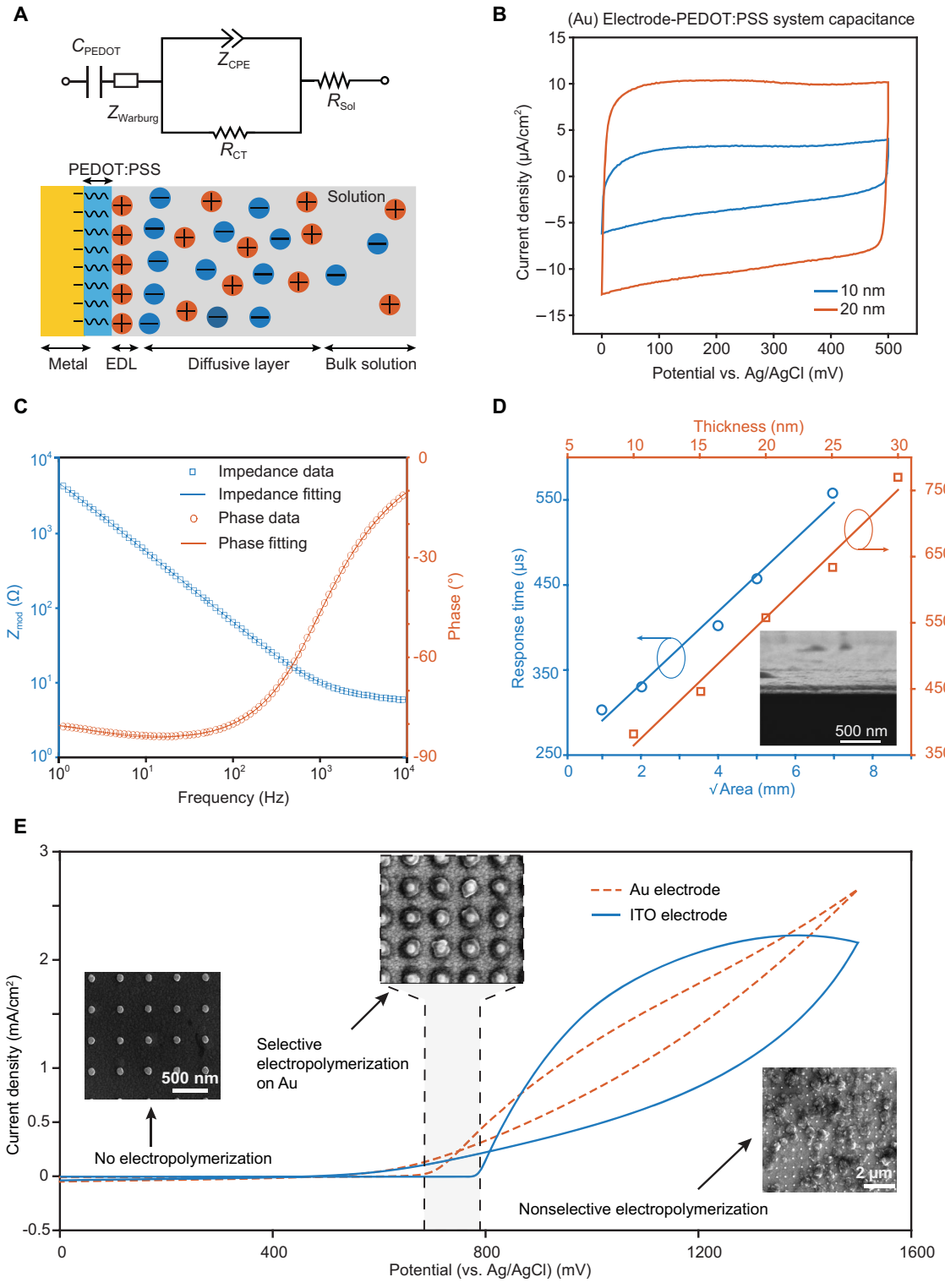

Fig. 2. Electrochromic loading. (**A**) Equivalent circuit model of the (Au) electrode-PEDOT:PSS system used in EIS measurement (top). PEDOT:PSS layer electropolymerized on an Au surface is illustrated in an electrolyte solution (bottom). (**B**) Cyclic voltammograms of 10-nm-thick (blue curve) and 20-nm-thick (red curve) PEDOT:PSS-coated Au electrodes. (**C**) Bode impedance plot of the (Au) electrode-PEDOT:PSS system. Excellent agreement is observed between EIS measurements and the equivalent circuit model. (**D**) Potential step voltammetry measurements to analyze the temporal response of the PEDOT:PSS film. Linear scaling of the electrochromic switching speed with the active area for fixed thickness t = 20 nm (blue curve) and thickness for fixed area √Area = 7 mm (red curve) is shown. Our electrochemical analysis suggests that it is advantageous to use a thinner and smaller surface area PEDOT:PSS load to achieve fast response times. (**E**) Selective electropolymerization of EDOT monomer in NaPSS aqueous solution under potentiostatic conditions. First, CV is used to characterize electropolymerization of PEDOT:PSS on Au (red curve) and ITO (blue curve) substrates. The nucleation point difference between Au and ITO surfaces is exploited for selective deposition of PEDOT:PSS on Au nanoantenna (insets).

constants, the (Au) electrode-PEDOT:PSS system is mapped to an equivalent circuit model (Fig. 2A) consisting of solution resistance R_{sol}, PEDOT:PSS layer electronic bulk capacitance C_{PEDOT}, finite-length Warburg diffusion impedance $Z_{Warburg}$, charge transfer resistance R_{CT}, and a constant phase element Z_{CPE}. $Z_{Warburg}$ is controlled by the diffusional time constant τ_D and the diffusional pseudo-capacitance C_D (Materials and Methods). We performed EIS measurements to obtain electrochemical circuit parameters and demonstrated an excellent agreement in between our circuit model and electrochemical measurements for a broad frequency range spanning from 1 Hz to 10 kHz (Fig. 2C, fig. S5, and table S1). Our analysis reveals that the capacitance of the PEDOT:PSS layer dominates impedance characteristics of the electrode-PEDOT:PSS system (table S1, top). Decreasing surface area reduces the diffusional pseudo-capacitance (C_D) and PEDOT:PSS electronic bulk capacitance (C_{PEDOT}), which control the temporal response of the (Au) electrode-PEDOT:PSS system (table S1, top); small–surface area PEDOT:PSS films respond to voltage changes much faster than the larger-area ones. Similarly, our circuit model predicts faster switching times with a thinner PEDOT:PSS load. As shown in our EIS measurements (table S1, bottom), this observation is associated to faster RC circuit response times due to the drastically lower diffusional pseudo-capacitance of the thinner (10 nm) PEDOT:PSS film (C_D = 0.177 mF). A substantially higher diffusional pseudo-capacitance (C_D = 2.26 mF) is observed for thicker films (20 nm). Subsequently, we performed PSV measurements to determine the response times for varying thicknesses of the PEDOT:PSS load and surface areas of the electrode-PEDOT:PSS system. A step voltage (+500 mV versus Ag/AgCl to +100 mV versus Ag/AgCl) is used in these experiments. The response time is calculated from the recorded electrical current. It is defined as the time during which current falls to 37% of its maximum value. In agreement with our circuit model predictions, linear scaling of the switching time with the active area of the electrode-PEDOT:PSS system is shown for a fixed-thickness (20 nm) PEDOT:PSS load (Fig. 2D, blue curve). Similarly, for a fixed-area ($\sqrt{\text{Area}}$ = 7 mm) electrode-PEDOT:PSS system, we observed that the electrochromic response time is linearly proportional with electrochromic load thickness (Fig. 2D, red curve). Accordingly, our electrochemical impedance analysis demonstrates that the temporal response of the PEDOT:PSS load can be drastically improved with lateral and vertical downscaling.

Following our electrochemical analysis, to achieve high-speed electrophysiological signal detection, we developed a selective electropolymerization technique that enables us to coat a Au nanoantenna with ultrathin and conformal PEDOT:PSS polymer at nanoscale dimensions. A three-electrode glass cell system is used under potentiostatic conditions using an aqueous solvent of 10 mM EDOT monomer and 0.1 M NaPSS (Materials and Methods). First, the nucleation potentials for the electropolymerization process are determined for the gold (Fig. 2E, red curve) and ITO (Fig. 2E, blue curve) surfaces with CV measurements (scan rate, 50 mV/s). As shown in Fig. 2E (left inset), no electropolymerization is observed for voltages below 675 mV. For voltages between 675 and 780 mV, polymerization initiates from the Au surface. In Fig. 2E (middle inset), an SEM image demonstrating the selective electrodeposition of PEDOT:PSS at 760 mV is shown. For electrodeposition voltages above 780 mV, both gold nanoantenna and ITO substrate are coated with PEDOT:PSS. In agreement with our CV measurements, nonselective electropolymerization is observed at a deposition voltage of 810 mV (Fig. 2E, right inset). Following an iterative procedure consisting of CV measurements and SEM imaging, we optimized our selective PEDOT:PSS loading technique and demonstrated reliable and conformal electrodeposition of ultrathin PEDOT films (down to 10 nm) with ultrasmall footprint (~0.01 μm^2) (Materials and Methods).

Ultrasensitive electric-field detection

During a cellular firing event, the membrane potential of an electrogenic cell (e.g., neurons or cardiomyocytes) experiences large fluctuations as a result of Na^+ influx into the cell (spike phase) and K^+ efflux from the cell (repolarization phase). These charge density (ion concentration) perturbations could give rise to strong transient electric fields. Field values as high as 10^5 V/cm are observed across membrane layers (*31*), while two to three orders of magnitude lower values (10^2 to 10^3 V/cm) are detected in the extracellular environment and within the synaptic regions with extremely small ion currents (~10 pA) (*32*). To determine the field sensitivity of our electro-plasmonic nanoantenna, we performed electro-optic measurements with controlled electric fields generated through a transparent counter electrode (Fig. 3A). For our sensitivity tests, we used a relatively low electric-field range (10^2 to 10^3 V/cm) that is comparable to the extracellular fields generated during electrogenic cell firing events (*32*). Intensity-based scattering measurements are obtained in transmission configuration using a laser beam that is focused to a diffraction-limited spot with an extra-long working-distance objective (Materials and Methods). The laser diode is modulated at a frequency of 500 Hz, and the scattered light from the electro-plasmonic nanoantenna is detected with an amplified photodetector connected to a lock-in amplifier (fig. S6 and Materials and Methods). In our experiments comparing pristine and loaded nanoantennas, the zero-bias scattering signal (S_0) and the electric field–modulated change in the scattering signal (ΔS) are monitored to obtain differential scattering signals ($\Delta S/S_0$). For the pristine nanoantenna, the differential scattering signal is shown to linearly increase with applied electric field at a rate of $(\Delta S/S_0E)^P = 2.8 \times 10^{-8}$ cm/V, in agreement with previous experimental studies (*13*). We demonstrated ~3.25×10^3-fold enhanced sensitivity of $(\Delta S/S_0E)^{EP} = 9.1 \times 10^{-5}$ cm/V for the electro-plasmonic nanoantenna. The high field sensitivities of our electro-plasmonic nanoantenna also favorably compare with those of quantum dot (QD) electric-field probes that have been recently used for monitoring the electrophysiological activity of neural cells (*6*). Using the electro-plasmonic nanoantenna, we demonstrated large scattering intensity changes of ~7% for low field values of 8×10^2 V/cm. QDs using the quantum-confined Stark effect, on the other hand, provide ~11% change in photoluminescence signals for an applied field of 10^5 V/cm, a field sensitivity that is nearly two orders of magnitude lower than that of electro-plasmonic nanoantenna (*6*, *7*, *33*).

To gain insight for drastically enhanced electric-field sensitivity with PEDOT:PSS loading, we developed an analytical model of the electro-plasmonic nanoantenna using quasi-static approximation (texts S2 to S4). We show that the spectral shifting of the resonances (through coupled electrochromic load) can be expressed as

$$\Delta\lambda_{LSP}^{EP} = \frac{\omega_p^2 \lambda_{LSP}^3}{8\pi^2 c^2}\left[\frac{(1-L)/L}{\left(\varepsilon_\infty + \varepsilon_{PEDOT}\left(\frac{1-L}{L}\right)\right)^2}\right]\Delta\varepsilon_{PEDOT} \quad (1)$$

where L is the geometrical factor for the nanoantenna, ω_p is the metal plasma frequency, λ_{LSP} is the plasmonic resonance wavelength, c is the speed of light, ε_∞ is the high-frequency contribution to metal dielectric

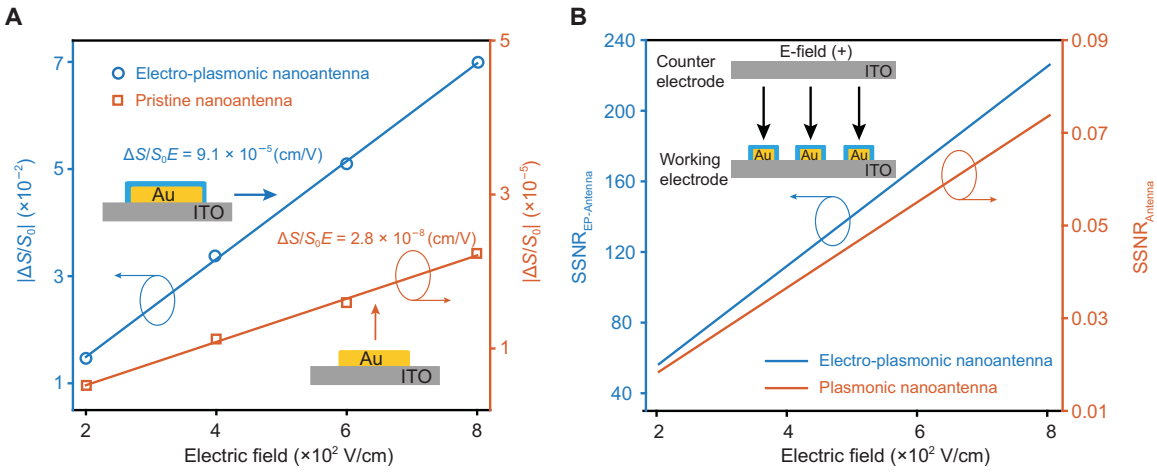

Fig. 3. Field sensitivity and signal-to-noise ratio. (**A**) Differential scattering signal versus applied electric-field strength. Electro-optic measurements are performed at a modulation frequency of 500 Hz. Absolute values of the differential scattering signals are compared for the pristine (red curve) and electro-plasmonic (blue curve) nanoantennas. Approximately 3.25×10^3 times enhanced field sensitivity is shown for the electro-plasmonic nanoantenna. For low field values (2×10^2 to 8×10^2 V/cm), we observed large intensity changes (1 to 7%) in scattering signal of the electro-plasmonic nanoantenna. (**B**) Detection limits of single electro-plasmonic and plasmonic nanoantennas. SSNR ratios are compared for single field probes at an illumination intensity of 300 W/cm^2. An integration time of 1 ms is considered. High SSNRs (~60 to 220) are shown for the electro-plasmonic nanoantenna even for low field values (2×10^2 to 8×10^2 V/cm). Reference field direction corresponding to positive electric-field is shown (inset).

function, and ε_{PEDOT} is the dielectric constant of the PEDOT:PSS film. Here, the resonance wavelength shift $\Delta\lambda_{LSP}^{EP}$ is proportional to $\Delta\varepsilon_{PEDOT}$, the change in the PEDOT:PSS permittivity with electric field. Our analytical model captures all prominent experimental observations. (i) The linear relationship between differential signal change and local electric-field strength, a crucial characteristic needed for quantitative detection of local electric-field strength, is associated to alteration of plasma frequency and linear modulation of the dielectric permittivity with electric field ($\Delta\varepsilon_{PEDOT} \propto E_{local}$ as shown in eqs. S15 and S16). (ii) A negative voltage applied to pristine nanoantenna stiffens the resonant free electron spring (plasma frequency of the metal) and blue shifts the localized surface plasmon (LSP) resonance to higher frequencies ($\Delta\lambda_P \propto E_{local}$). This observation is opposite in the case of electro-plasmonic nanoantenna, where a negative voltage causes red shifting of the LSP resonances ($\Delta\lambda_{EP} \propto -E_{local}$) (*16*). Reversal of the resonance wavelength shift direction with PEDOT:PSS loading is explained in our model through the electric field–induced modulation of the PEDOT:PSS plasma frequency, which is much larger than that of the pristine nanoantenna (eq. S10 versus eq. S17). (iii) Our model shows that the large difference in electron densities of Au (~10^{23}cm^{-3}) (*15*) and conducting polymer PEDOT:PSS (~5.3×10^{18}cm^{-3}) (*34*) materials is responsible for the experimentally observed drastic sensitivity enhancement. The calculated values of sensitivity improvement with electrochromic loading $(\Delta S/SE)^{EP}/(\Delta S/SE)^{P} \approx -(N_{Au}/N_{PEDOT})^{5/6} \approx 3.66 \times 10^3$ are in close agreement with those measured experimentally, ~3.25×10^3 (Fig. 3A).

High SSNR recordings with single electro-plasmonic nanoantenna

The fundamental limit to any optical measurement technique is the shot noise. SSNR is proportional to the ratio of signal change, ΔS, and the baseline shot noise ($S_0/\sqrt{N_{ph}}$, where N_{ph} is the number of photons detected): SSNR ~ $(\Delta S/S_0)\sqrt{N_{ph}}$. Hence, high field sensitivity ($\Delta S/S_0E$) probes providing high photon counts (N_{ph}) are needed to achieve reliable measurement of the electric-field dynamics with light. Typically, a small number of photons are detected from small structures, such as fluorescence molecules and QD field probes. In contrast, LSP-mediated light scattering from the electro-plasmonic nanoantenna leads to orders of magnitude higher photon counts. Plasmon-enhanced cross sections of our electro-plasmonic nanoprobes are ~3.6×10^4 nm^2 compared to typical values of ~10^{-2} nm^2 for GEVIs (*27*, *29*) and ~1 nm^2 for QDs (*7*, *33*). We calculated SSNRs for our electro-plasmonic nanoantenna for varying electric-field strengths. In our calculations, we used our experimentally obtained differential signal values, typical light intensities (300 W/mm^2) used in fluorescence measurements, and scattering cross sections obtained from our FDTD simulations (fig. S7). As shown in Fig. 3B (blue curve), a single electro-plasmonic antenna enables optical detection of local field dynamics at 1 kHz with a remarkably high SSNR of ~60 to 220 for low field values of 2×10^2 to 8×10^2 V/cm. This high SSNR measurement capability, outperforming whole-cell body voltage-sensitive fluorescence measurements (*2*), paves the way to extracellular voltage measurements from diffraction-limited spots. Further improvements in photon counts and SSNRs can be achieved by packing higher number of electro-plasmonic nanoantenna within a diffraction-limited spot size. Our SSNR calculations also reveal the strong contribution of electrochromic load for reliable detection of electrical signals with light. As shown in Fig. 3B (red curve), with conventional plasmonic nanoantennas, SSNRs are far below the theoretical detection limits (SSNR < 0.1), preventing reliable measurement of electric-field dynamics with high spatial resolution.

Optoelectrochemical measurements and high-bandwidth detection

We determined the optical response times of our electro-plasmonic through in situ optoelectrochemical testing using a custom-built three-electrode electrochemical cell. In our measurements, electro-plasmonic nanoantenna substrate is used as the working electrode. We obtained the far-field scattering signal of the electro-plasmonic nanoantenna using a dark-field transmission setup illustrated in Fig. 4A. Here, the high [numerical aperture (NA), 0.8 to 0.95] condenser is used for sample

illumination through a hollow cone. The low NA objective (20×; NA, 0.45) is designed to collect only the scattered light, which is continuously recorded with an amplified photodetector at a gain (Hi-Z) of 4.75×10^6 V/A ± 5%. To obtain the temporal response of the electro-plasmonic nanoantenna, a square wave voltage (−500 to 500 mV, 100 Hz) is applied using a potentiostat (Gamry reference 600). The response time of our electro-plasmonic nanoantenna is determined by fitting a decaying exponential function to the scattered optical signal. In our experiments, we demonstrated submillisecond response times (~191 μs) sufficient to resolve electrogenic activity of cells (Fig. 4B). We also proved the high-bandwidth functionality of our electro-plasmonic nanoantenna at kilohertz frequencies (fig. S8). Our in situ optoelectrochemical experiments also confirmed the excellent stability and reversible response of ultrathin and nanoscale electrochromic load over millions of switching cycles.

In vitro optical detection of electrogenic signals

We demonstrated the in vitro functionality of our field probes for label-free optical detection of electrophysiological activity of the excitable cells. In our experiments, stem cell–derived iCMs are used (Materials and Methods) (*35*). Before electro-optic testing, iCMs are seeded at a density of 2×10^6 cells/ml on a fibronectin-coated electro-plasmonic nanoantenna array (Fig. 4C), and their electrophysiological functionality is confirmed using Ca^{2+} indicators (Materials and Methods and fig. S9). The electro-plasmonic nanoantenna (~3.6×10^4 nm^2) has more than few million times larger cross sections than the GEVIs (~10^{-2} nm^2) (*8*). Thus, the light intensities used in our experiments (11 mW/mm^2) were ~10^2 to 10^3 times lower than the typical excitation sources used in optical experiments with fluorescence molecules (*2*, *5*). To assure that the optical signal is a result of electrical activity only, a myosin II inhibitor, blebbistatin (10 μM), is used (*36*, *37*). Blebbistatin prevents mechanical motion (i.e., contractions) of the cardiac cells, as shown in movie S1 (before blebbistatin) and movie S2 (after blebbistatin). Using fast Ca^{2+} imaging, we confirmed that the addition of blebbistatin does not interfere with the electrophysiological activity of cells (movie S3). In our network-level experiments, the scattering signal is continuously collected using a 20× objective in transmission dark-field measurement configuration (Fig. 4A) and a spectrometer (Ocean Optics, HR4000) with 50-ms integration time. Photon counts are obtained following a spectral integration method as a function of time (Fig. 4D). Our measurements show that the electrogenic activity of spontaneously firing iCMs leads to increased light scattering (Fig. 4D,

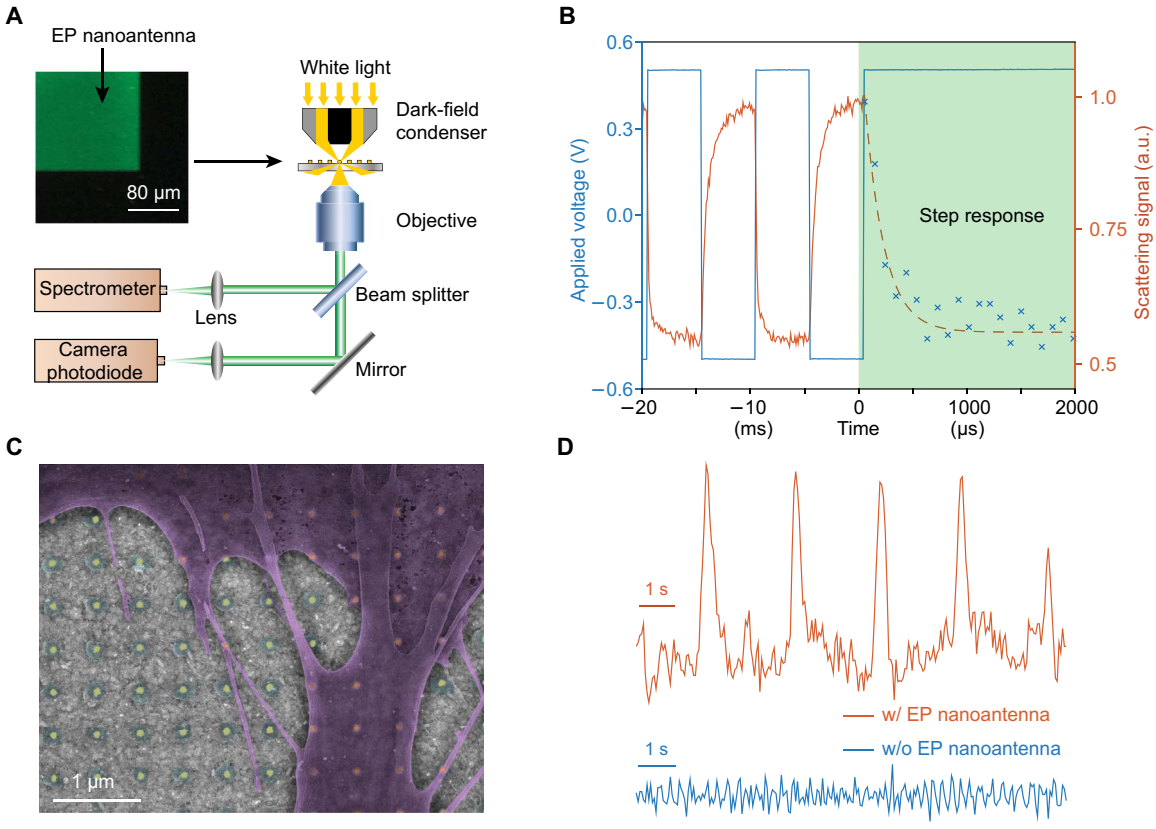

Fig. 4. Optical recording of electrogenic activity. (**A**) Schematics of the transmission dark-field measurement setup. Strong light scattering contrast in between the spatial regions with (green) and without (dark) electro-plasmonic (EP) nanoantenna is observed (inset). (**B**) Temporal response of the electro-plasmonic nanoantenna obtained using a square wave voltage for spectroelectrochemical recording. Optical response of the electro-plasmonic nanoantenna is shown (red curve) for potential steps (blue curve) in between −500 mV (versus Ag/AgCl) and 500 mV (versus Ag/AgCl) with a residence time of 5 ms. A switching time of 191 μs is obtained after fitting a decaying-exponential function to the scattered light intensity. (**C**) False-color scanning electron micrograph of hiPSC-derived iCMs (colored purple) cultured on electro-plasmonic nanoantenna array. (**D**) Differential scattering signal in response to electrogenic activity of a network of cardiomyocyte cells. Strong far-field signal allowing label-free and real-time optical detection of electrogenic activity of iCMs is obtained from substrates with electro-plasmonic nanoantennas (red curve). Control measurements are performed to verify the origin of the electro-optic signal. In the absence of electro-plasmonic nanoantennas, no far-field signal is detected (blue curve).

red curve). This observation is in strong agreement with our optoelectrochemical measurements, as spontaneous depolarization of cardiomyocytes (Na^+ influx into the cell) results in a transient electric field directed toward the electro-plasmonic nanoantennas (as in Fig. 3B, inset). To verify the electro-plasmonic origin of the label-free and real-time optical signal, measurements are repeated with iCMs cultured on substrates without the electro-plasmonic nanoantenna. No far-field optical signal for the cellular firing events is observed in the absence of the electro-plasmonic nanoantenna (Fig. 4D, blue curve). We theoretically investigated the local temperature increase as a result of photothermal heat generation during our experiments (text S6). Our analysis shows that the temperature increase is limited (<3°C) and confined at the nanoscale vicinity (<10 nm) of the electro-plasmonic nanoantenna. As shown in fig. S10, plasmon-assisted temperature increase is too low to cause any thermal damage to cardiomyocyte cells. Furthermore, no phototoxic effect of light is observed during our experiments. Phototoxicity is an important concern for the viability of fluorescently labeled cells (*1*, *4*); fluorescence excitation always produces disruptive oxygen free radicals (*38*). Extracellular electro-plasmonic nanoantennas, on the other hand, use a different optical signaling mechanism from fluorescence excitation. In addition, the light intensities used in our experiments are much lower than those used in fluorescence-based measurements.

DISCUSSION

We introduced an extremely bright electro-plasmonic field probe offering ultrasensitive and label-free detection of electrical signals at kilohertz frequencies with light. To achieve this, we developed a novel electropolymerization technique enabling us to exploit biocompatible electrochromic polymer PEDOT:PSS as an electric field–controlled ultrathin and nanoscale optical load. Existing optical field probes run into signal-to-noise ratio limitations due to either low photon counts (e.g., GEVIs) or low electric-field sensitivities (e.g., QDs and plasmonic nanoantenna). In our experiments, we demonstrated that the electro-plasmonic nanoantenna enables optical transduction of local field dynamics with more than ~3.25×10^3 times enhanced field sensitivities over conventional plasmonic nanoantennas (*13*) and nearly two orders of magnitude higher-intensity modulations over QD field probes (*6*, *7*). Furthermore, enhanced cross sections (~3.6×10^4 nm^2) of our electro-plasmonic nanoprobes are orders of magnitude larger than those of GEVIs (~10^{-2} nm^2) (*8*) and QDs (~1 nm^2) (*7*, *33*). By merging high field sensitivity and photon counts together, we show that our electro-plasmonic probes offer remarkably high SSNR (~60 to 220) measurement capability from diffraction-limited spots. Our study also includes the first practical uses of electro-plasmonic field probes for in vitro electrophysiological tests at the network level. By tracking the far-field spectral response of our field probes, we demonstrated real-time label-free detection of spiking activity of cardiomyocyte cells with low-intensity light (11 mW/mm^2).

Beyond the in vitro experiments performed here, our electro-plasmonic probes open the possibility of in vivo electrophysiological studies with high SSNRs for prolonged periods. Our theoretical analysis, in strong agreement with our experimental observations, confirms that the electrochromic loading effects are fully responsible for the differential signal modulation with electric field and drastic enhancement of field sensitivities (see text S3). Surface immobilization of our electro-plasmonic probes on conducting ITO substrate, although helpful during nanofabrication and electrochemical characterization processes, is not needed for our electric-field probing mechanism to work. For in vivo electrophysiological testing, it is possible to use our electro-plasmonic probes using two distinct approaches: (i) Electro-plasmonic probes can be integrated on flexible and biocompatible substrates for surgical implantation, and (ii) colloidal versions of them can be synthesized and functionalized with cell-specific biomolecules for deep tissue brain imaging. Several recent studies have already demonstrated integration of plasmonic devices on flexible substrates and optical fibers using high-throughput fabrication techniques (*39*, *40*). For deep tissue use, high-quality colloidal plasmonic nanoparticles can be synthesized in solution (*41*) and loaded with electrochromic polymers using electrostatic oxidative polymerization (*42*). Furthermore, biocompatible PEDOT polymer enables surface functionalization with proteins for tethering colloidal electro-plasmonic nanoprobes to specific cell types (*30*). A similar approach has been successfully used for interfacing extracellular QDs to a range of cell lines, including neurons (*6*). An important consideration for in vivo applications is the light scattering and absorption in tissue. Electrochromic properties of PEDOT polymer are manifested over a broad wavelength spectrum spanning well into near-infrared wavelengths (*25*). Using spherically symmetric core-shell plasmonic structures (*41*) loaded with electrochromic polymers, it is possible to operate electro-plasmonic probes at near-infrared wavelengths, which is particularly amenable for in vivo applications owing to reduced photon scattering and absorption in deep tissue as shown in a recent study (*43*). Another important consideration for in vivo probes is the inherent immune response. In this respect, electro-plasmonic nanoparticles offer two important advantages. PEDOT films functionalized with bioactive molecules are shown to markedly minimize immune response and enable in vivo recording of electrical activity for long time periods (*30*). Moreover, probe dimensions that are smaller than 12 μm are shown to induce minimal reactive cell responses (*29*). In this sense, nanoscale dimensions of our polymer-coated electro-plasmonic probes are particularly advantageous for long-term operation.

MATERIALS AND METHODS

Fabrication of plasmonic nanoantenna arrays

Plasmonic nanoantenna arrays were fabricated using electron beam lithography (EBL) followed by a liftoff process (fig. S1). To minimize charging effects during EBL, high-conductivity (8 to 12 Ω/cm) ITO glass slides (Structure Probe Inc.) were used. Initially, ITO glass slides were cleaned in sonication bath of acetone and isopropyl alcohol for 5 min. Immediately after removal from the final sonication bath, the slides were blow-dried using nitrogen. A poly(methyl methacrylate) 495A4 (Microchem) electron-beam resist was spin-coated at 4000 rpm and baked on a hot plate at 180°C for 90 s. EBL is performed using FEI Quanta 3D FEG SEM with an accelerating voltage of 30 kV. An electron-beam–exposed resist was developed for 1 min in a methyl isobutyl ketone (MIBK):isopropanol (IPA) solution (MIBK:IPA = 1:3) for 60 s, rinsed in IPA for 1 min, and blow-dried with nitrogen. A 45-nm-thick gold layer (Kurt J. Lesker, 99.999% purity) was evaporated on the developed substrates using a custom-built electron-beam evaporator. The deposition was carried out at a pressure of 1.2×10^{-6} torr and an evaporation rate of 0.5 Å/s. In the final step, the resist was removed through a liftoff process with acetone and IPA, leaving behind the pristine plasmonic nanoantenna array on the ITO-coated glass substrate.

Full-wave numerical simulations

Pristine and electro-plasmonic nanoantenna arrays were modeled using a full-wave FDTD solver provided by Lumerical Inc. The "Au

(Gold)–CRC" dielectric constants were used for gold structures (*44*). The complex dielectric constants of PEDOT load (fig. S2) were obtained using Kramers-Kronig relation from a previous experimental study (*25*). Perfectly matched layer boundary conditions were used in the vertical direction. A linearly polarized excitation source (400 to 900 nm) was used in our simulations.

Electropolymerization of ultrathin PEDOT:PSS polymer

Electropolymerization of electrochromic polymer PEDOT:PSS was performed using a three-electrode configuration. A custom-made platinum coil (Alfa Aesar, 13039) and Ag/AgCl (Warner Instruments, 64-1282) were used as the counter electrode and reference electrodes, respectively. Conducting substrate was used as the working electrode. An aqueous solvent of 10 mM EDOT monomer and 0.1 M NaPSS was deposited using a galvanostatic approach. A constant current of 0.48 mA/cm^2 was applied for 1.67 s for each 5-nm PEDOT:PSS film (fig. S4). Electropolymerization process was confirmed by CV measurements in 0.1 M $TBAPF_6$ (Sigma-Aldrich, 281026) in propylene carbonate solution (Sigma-Aldrich, 310328). Selective deposition of PEDOT:PSS on the Au surface was achieved using the same aqueous solvent solution under potentiostatic conditions (740 mV versus Ag/AgCl) for 6.5 s.

EIS characterization of the (Au) electrode-PEDOT:PSS system

An equivalent circuit model of the (Au) electrode-PEDOT:PSS system was developed (Fig. 2A) using electrochemical measurements. In this model, the finite-length Warburgh diffusion impedance (Z_{Warburg}) is defined as (*45*)

$$Z_{\mathrm{Warburg}} = \frac{1}{Y_0\sqrt{j\omega}}\coth(j\omega\tau_D)^{1/2} \quad (2)$$

where ω is the frequency and Y_0 is the frequency-independent admittance $Y_0 = C_D(\tau_D)^{-1/2}$. Electrical impedance spectroscopy (EIS) measurements were used to find the circuit parameters. Impedance spectra were recorded by applying a sinusoidal excitation signal with an excitation amplitude of 10 mV (rms) that is superimposed on a constant dc potential of 200 mV. Frequency-dependent electronic response of the Au electrode-PEDOT:PSS system was fitted to an equivalent circuit model. Circuit parameters were obtained using Echem Analyst software.

Electro-optic characterization

To characterize pristine and electro-plasmonic nanoantennas, a custom-built electro-optic measurement platform based on an inverted microscope (Nikon TE2000-U) was used (fig. S6A). Its schematic is shown in fig. S6B. Electro-optics measurements were performed using a 670-nm diode temperature-stabilized laser modulated at a frequency of 500 Hz (for synchronous detection of scattering signal using lock-in amplifier). The laser was focused onto the nanoparticles at normal incidence using 40× Nikon S Plan Fluor ELWD objective (NA = 0.6). The forward scattering light was collected using a custom collection optics with 50° to the normal using a collection optics consisting of a 20× infinity-corrected objective (NA = 0.4) with a front aperture of 3 mm, a fiber collimator, and a 600-μm multimode optical fiber patch cable. The collected light was measured using a fiber-coupled silicon photodetector (Thorlabs, PDA100A). A lock-in amplifier (Stanford Research Systems, SR850) connected to an oscilloscope (Rigol, DS4034) was used for detection. To characterize the voltage-dependent scattering response (electric-field sensitivity) of the nanoantenna, a second ITO-covered glass slide was used as the counter electrode. The separation between electrodes was set to 100 μm using a polydimethylsiloxane spacer layer. A function generator (Rigol, DG4102) was used to control the applied voltage difference (electric field) between electrodes. The voltage-dependent ac scattering signal was measured using the lock-in amplifier, while the dc component of the scattering signal was monitored using the oscilloscope.

Stem cell culture

1016SevA line hiPSCs were cultured on Geltrex (1%; Invitrogen, USA)–coated culture flasks in mTeSR1 media (STEMCELL Technologies, Canada) supplemented with penicillin and streptomycin (P/S) (1%; Life Technologies, USA). hiPSCs were passaged using Accutase (STEMCELL Technologies, Canada) to detach, at approximately 70% confluency, and seeded with Rho-associated, coiled-coil containing protein kinase inhibitor (5 μM; STEMCELL Technologies, Canada)–supplemented mTeSR1. The culture was kept with daily media changes until 70% confluency for passaging or 95% confluency for differentiation.

Cardiomyocyte differentiation, maintenance, and Ca^{2+} imaging

hiPSC-derived iCM differentiation induction was adapted from a previously established protocol (*35*, *46*, *47*). Briefly, RPMI medium 1640 (Life Technologies, USA) was supplemented with β-mercaptoethanol (3.4×10^{-4}%; Promega, USA), P/S (1%), and B27 without any insulin (2%; Invitrogen, USA) [CM (−)] or B27 (2%, Invitrogen, USA) [CM (+)]. On day 1, hiPSC media were replaced with CM (−) media with the addition of Wnt activator CHIR99021 (CHIR) (10 μM; Stemgent, USA). On day 2, 24 hours after the differentiation was initiated, media were changed to CM (−). On day 4, iCMs were treated with Wnt inhibitor IWP-4–supplemented (10 μM; Stemgent, USA) CM (−) media. On day 6, the media were changed to CM (−) again. Starting from day 9 onward, media were changed every 3 days with CM (+). On day 35, iCMs were collected using trypsin-EDTA (0.25%; Corning, USA) and reseeded on fibronectin in phosphate-buffered saline (50 μg/ml; Sigma-Aldrich, USA)–coated substrates. iCM cultures were then maintained in Dulbecco's modified Eagle's medium (DMEM; Hyclone, USA) supplemented with fetal bovine serum (10%; Hyclone, USA) and P/S (1%) (DMEM). The functionality of iCMs was confirmed using Ca^{2+} indicators. iCMs were loaded with Fluo-4 acetoxymethy ester (Molecular Probes), which exhibits an increase in fluorescence intensity upon binding to Ca^{2+}, following the manufacturer's instructions. Briefly, iCMs were incubated in Tyrode's salt solution (Sigma-Aldrich) loaded with 3 μM Fluo-4 acetoxymethy ester and 0.02% Pluronic F127 (Life Technologies), incubated at 37°C for 30 min, washed with Tyrode's salt solution, and kept in normal culture medium. Ca^{2+} fluxing during spontaneous contractions were captured using high-speed fluorescence microscope imaging (Axio Observer Z1, Carl Zeiss).

SEM imaging of cardiomyocytes

For SEM imaging, cells were fixed for 1 hour using 2% glutaraldehyde (Sigma-Aldrich, USA) in sodium cacodylate buffer (Sigma-Aldrich, USA). Then, another fixation step was performed for 1 hour using 1% osmium tetroxide in sodium cacodylate followed by dehydration in 10% ethanol. Last, critical point drying was performed, and samples were attached to an SEM stub. Figure 1A shows the SEM micrograph of an iCM on top of an electro-plasmonic nanoantenna array.

SUPPLEMENTARY MATERIALS

Supplementary material for this article is available at http://advances.sciencemag.org/cgi/content/full/5/10/eaav9786/DC1

Text S1. Optical circuit model.
Text S2. Pristine plasmonic nanoantenna response to electric field.
Text S3. Electro-plasmonic nanoantenna response to electric field.
Text S4. Sensitivity enhancement with electrochromic loading.
Text S5. SSNRs obtained using a single electro-plasmonic nanoantenna.
Text S6. Photothermal heating.
Fig. S1. Fabrication steps of electro-plasmonic nanoantenna arrays.
Fig. S2. Complex refractive index (*n-k*) of the PEDOT polymer.
Fig. S3. Lumped optical circuit model of pristine nanoantenna.
Fig. S4. Electropolymerization of nanometer-thick PEDOT:PSS films.
Fig. S5. Impedance spectroscopy of PEDOT:PSS on gold.
Fig. S6. Electro-optic characterization setup.
Fig. S7. Scattering spectra of pristine and electro-plasmonic nanoantenna.
Fig. S8. Dynamic response of the electro-plasmonic field probe.
Fig. S9. Ca^{2+} flux of iCMs captured using fast Ca^{2+} imaging.
Fig. S10. Photothermal heating due the nanoantenna.
Table S1. EIS obtained equivalent circuit parameters of PEDOT:PSS-coated gold electrodes.
Table S2. Parameters used in the SSNR calculation.
Movie S1. Bright-field recording of iCMs before blebbistatin application.
Movie S2. Bright-field recording of iCMs after blebbistatin application.
Movie S3. Ca^{2+} flux of iCMs captured using fast Ca^{2+} after blebbistatin application.
References (*48*–*54*)

REFERENCES AND NOTES

1. M. Scanziani, M. Häusser, Electrophysiology in the age of light. *Nature* **461**, 930–939 (2009).
2. D. R. Hochbaum, Y. Zhao, S. L. Farhi, N. Klapoetke, C. A. Werley, V. Kapoor, P. Zou, J. M. Kralj, D. Maclaurin, N. Smedemark-Margulies, J. L. Saulnier, G. L. Boulting, C. Straub, Y. K. Cho, M. Melkonian, G. K.-S. Wong, D. J. Harrison, V. N. Murthy, B. L. Sabatini, E. S. Boyden, R. E. Campbell, A. E. Cohen, All-optical electrophysiology in mammalian neurons using engineered microbial rhodopsins. *Nat. Methods* **11**, 825–833 (2014).
3. E. S. Boyden, Optogenetics and the future of neuroscience. *Nat. Neurosci.* **18**, 1200–1201 (2015).
4. V. Emiliani, A. E. Cohen, K. Deisseroth, M. Häusser, All-optical interrogation of neural circuits. *J. Neurosci.* **35**, 13917–13926 (2015).
5. T. Knöpfel, J. Díez-García, W. Akemann, Optical probing of neuronal circuit dynamics: Genetically encoded versus classical fluorescent sensors. *Trends Neurosci.* **29**, 160–166 (2006).
6. A. L. Efros, J. B. Delehanty, A. L. Huston, I. L. Medintz, M. Barbic, T. D. Harris, Evaluating the potential of using quantum dots for monitoring electrical signals in neurons. *Nat. Nanotechnol.* **13**, 278–288 (2018).
7. J. D. Marshall, M. J. Schnitzer, Optical strategies for sensing neuronal voltage using quantum dots and other semiconductor nanocrystals. *ACS Nano* **7**, 4601–4609 (2013).
8. L. Kastrup, S. W. Hell, Absolute optical cross section of individual fluorescent molecules. *Angew. Chem. Int. Ed. Eng.* **43**, 6646–6649 (2004).
9. Y. Huang, M. C. Pitter, M. G. Somekh, Time-dependent scattering of ultrathin gold film under potential perturbation. *ACS Appl. Mater. Interfaces* **4**, 3829–3836 (2012).
10. Y. Huang, M. C. Pitter, M. G. Somekh, Morphology-dependent voltage sensitivity of a gold nanostructure. *Langmuir* **27**, 13950–13961 (2011).
11. S. Ae Kim, K. Min Byun, J. Lee, J. Hoon Kim, D.-G. Albert Kim, H. Baac, M. L. Shuler, S. June Kim, Optical measurement of neural activity using surface plasmon resonance. *Opt. Lett.* **33**, 914–916 (2008).
12. S. A. Kim, S. J. Kim, H. Moon, S. B. Jun, In vivo optical neural recording using fiber-based surface plasmon resonance. *Opt. Lett.* **37**, 614–616 (2012).
13. J. Zhang, T. Atay, A. V. Nurmikko, Optical detection of brain cell activity using plasmonic gold nanoparticles. *Nano Lett.* **9**, 519–524 (2009).
14. P. K. Jain, K. S. Lee, I. H. El-Sayed, M. A. El-Sayed, Calculated absorption and scattering properties of gold nanoparticles of different size, shape, and composition: Applications in biological imaging and biomedicine. *J. Phys. Chem. B* **110**, 7238–7248 (2006).
15. X. Liu, J.-H. Kang, H. Yuan, J. Park, S. J. Kim, Y. Cui, H. Y. Hwang, M. L. Brongersma, Electrical tuning of a quantum plasmonic resonance. *Nat. Nanotechnol.* **12**, 866–870 (2017).
16. M. C. Pitter, J. Paul, J. Zhang, M. G. Somekh, in *SPIE BiOS* (SPIE, 2009), vol. 7180, p. 12.
17. A. Alù, N. Engheta, Input impedance, nanocircuit loading, and radiation tuning of optical nanoantennas. *Phys. Rev. Lett.* **101**, 043901 (2008).
18. A. Alù, N. Engheta, Tuning the scattering response of optical nanoantennas with nanocircuit loads. *Nat. Photonics* **2**, 307–310 (2008).
19. A. Alù, N. Engheta, Wireless at the nanoscale: Optical interconnects using matched nanoantennas. *Phys. Rev. Lett.* **104**, 213902 (2010).
20. M. Schnell, A. García-Etxarri, A. J. Huber, K. Crozier, J. Aizpurua, R. Hillenbrand, Controlling the near-field oscillations of loaded plasmonic nanoantennas. *Nat. Photonics* **3**, 287–291 (2009).
21. N. Liu, F. Wen, Y. Zhao, Y. Wang, P. Nordlander, N. J. Halas, A. Alù, Individual nanoantennas loaded with three-dimensional optical nanocircuits. *Nano Lett.* **13**, 142–147 (2012).
22. C. P. Byers, H. Zhang, D. F. Swearer, M. Yorulmaz, B. S. Hoener, D. Huang, A. Hoggard, W. S. Chang, P. Mulvaney, E. Ringe, N. J. Halas, P. Nordlander, S. Link, C. F. Landes, From tunable core-shell nanoparticles to plasmonic drawbridges: Active control of nanoparticle optical properties. *Sci. Adv.* **1**, e1500988 (2015).
23. N. Liu, M. L. Tang, M. Hentschel, H. Giessen, A. P. Alivisatos, Nanoantenna-enhanced gas sensing in a single tailored nanofocus. *Nat. Mater.* **10**, 631–636 (2011).
24. J. Li, S. Kamin, G. Zheng, F. Neubrech, S. Zhang, N. Liu, Addressable metasurfaces for dynamic holography and optical information encryption. *Sci. Adv.* **4**, eaar6768 (2018).
25. A. Baba, J. Lübben, K. Tamada, W. Knoll, Optical properties of ultrathin poly(3,4-ethylenedioxythiophene) films at several doping levels studied by in situ electrochemical surface plasmon resonance spectroscopy. *Langmuir* **19**, 9058–9064 (2003).
26. V. Jain, H. M. Yochum, R. Montazami, J. R. Heflin, Millisecond switching in solid state electrochromic polymer devices fabricated from ionic self-assembled multilayers. *Appl. Phys. Lett.* **92**, 033304 (2008).
27. N. Engheta, Circuits with light at nanoscales: Optical nanocircuits inspired by metamaterials. *Science* **317**, 1698–1702 (2007).
28. A. Elschner, *PEDOT: Principles and Applications of an Intrinsically Conductive Polymer* (CRC Press, 2011).
29. K. A. Ludwig, N. B. Langhals, M. D. Joseph, S. M. Richardson-Burns, J. L. Hendricks, D. R. Kipke, Poly(3,4-ethylenedioxythiophene) (PEDOT) polymer coatings facilitate smaller neural recording electrodes. *J. Neural Eng.* **8**, 014001 (2011).
30. X. Cui, D. C. Martin, Electrochemical deposition and characterization of poly(3,4-ethylenedioxythiophene) on neural microelectrode arrays. *Sens. Actuators B Chem.* **89**, 92–102 (2003).
31. C. Bédard, A. Destexhe, Macroscopic models of local field potentials and the apparent 1/f noise in brain activity. *Biophys. J.* **96**, 2589–2603 (2009).
32. S. Sylantyev, L. P. Savtchenko, Y. P. Niu, A. I. Ivanov, T. P. Jensen, D. M. Kullmann, M.-Y. Xiao, D. A. Rusakov, Electric fields due to synaptic currents sharpen excitatory transmission. *Science* **319**, 1845–1849 (2008).
33. S. A. Empedocles, M. G. Bawendi, Quantum-confined stark effect in single CdSe nanocrystallite quantum dots. *Science* **278**, 2114–2117 (1997).
34. Y. Du, X. Cui, L. Li, H. Tao, W.-X. Yu, Z.-X. Zhou, Dielectric properties of DMSO-Doped-PEDOT:PSS at THz frequencies. *Phys. Status Solidi B* **255**, 1700547 (2018).
35. B. W. Ellis, A. Acun, U. I. Can, P. Zorlutuna, Human iPSC-derived myocardium-on-chip with capillary-like flow for personalized medicine. *Biomicrofluidics* **11**, 024105 (2017).
36. G. P. Farman, K. Tachampa, R. Mateja, O. Cazorla, A. Lacampagne, P. P. de Tombe, Blebbistatin: Use as inhibitor of muscle contraction. *Pflugers Arch.* **455**, 995–1005 (2008).
37. J. Abbott, T. Ye, L. Qin, M. Jorgolli, R. S. Gertner, D. Ham, H. Park, CMOS nanoelectrode array for all-electrical intracellular electrophysiological imaging. *Nat. Nanotechnol.* **12**, 460–466 (2017).
38. P. P. Laissue, R. A. Alghamdi, P. Tomancak, E. G. Reynaud, H. Shroff, Assessing phototoxicity in live fluorescence imaging. *Nat. Methods* **14**, 657–661 (2017).
39. S. Aksu, M. Huang, A. Artar, A. A. Yanik, S. Selvarasah, M. R. Dokmeci, H. Altug, Flexible plasmonics on unconventional and nonplanar substrates. *Adv. Mater.* **23**, 4422–4430 (2011).
40. L. Gao, Y. Zhang, H. Zhang, S. Doshay, X. Xie, H. Luo, D. Shah, Y. Shi, S. Xu, H. Fang, J. A. Fan, P. Nordlander, Y. Huang, J. A. Rogers, Optics and nonlinear buckling mechanics in large-area, highly stretchable arrays of plasmonic nanostructures. *ACS Nano* **9**, 5968–5975 (2015).
41. E. Prodan, C. Radloff, N. J. Halas, P. Nordlander, A hybridization model for the plasmon response of complex nanostructures. *Science* **302**, 419–422 (2003).
42. J.-W. Jeon, P. A. Ledin, J. A. Geldmeier, J. F. Ponder Jr., M. A. Mahmoud, M. el-Sayed, J. R. Reynolds, V. V. Tsukruk, Electrically controlled plasmonic behavior of gold nanocube@polyaniline nanostructures: Transparent plasmonic aggregates. *Chem. Mater.* **28**, 2868–2881 (2016).
43. G. Hong, S. Diao, J. Chang, A. L. Antaris, C. Chen, B. Zhang, S. Zhao, D. N. Atochin, P. L. Huang, K. I. Andreasson, C. J. Kuo, H. Dai, Through-skull fluorescence imaging of the brain in a new near-infrared window. *Nat. Photonics* **8**, 723–730 (2014).
44. E. D. Palik, G. Ghosh, *Handbook of Optical Constants of Solids* (Academic Press, 1998).
45. J. Bobacka, A. Lewenstam, A. Ivaska, Electrochemical impedance spectroscopy of oxidized poly(3,4-ethylenedioxythiophene) film electrodes in aqueous solutions. *J. Electroanal. Chem.* **489**, 17–27 (2000).

46. A. Acun, T. D. Nguyen, P. Zorlutuna, An aged human heart tissue model showing age-related molecular and functional deterioration resembling the native heart. *bioRxiv* 10.1101/287334 (2018).
47. X. Lian, J. Zhang, S. M. Azarin, K. Zhu, L. B. Hazeltine, X. Bao, C. Hsiao, T. J. Kamp, S. P. Palecek, Directed cardiomyocyte differentiation from human pluripotent stem cells by modulating Wnt/β-catenin signaling under fully defined conditions. *Nat. Protoc.* **8**, 162–175 (2013).
48. N. Engheta, A. Salandrino, A. Alù, Circuit elements at optical frequencies: Nanoinductors, nanocapacitors, and nanoresistors. *Phys. Rev. Lett.* **95**, 095504 (2005).
49. Y. Zhao, N. Engheta, A. Alù, Effects of shape and loading of optical nanoantennas on their sensitivity and radiation properties. *J. Opt. Soc. Am. B* **28**, 1266–1274 (2011).
50. S. A. Maier, *Plasmonics: Fundamentals and Applications* (Springer, 2007).
51. K.-Y. Jung, W.-J. Yoon, Y. B. Park, P. R. Berger, F. L. Teixeira, Broadband finite-difference time-domain modeling of plasmonic organic photovoltaics. *ETRI J.* **36**, 654–661 (2014).
52. S. H. Chang, C. Chiang, F. Kao, C. Tien, C. Wu, Parasitic stimulated amplification in high-peak-power and diode-seeded nanosecond fiber amplifiers. *IEEE Photonics J.* **6**, 1–8 (2014).
53. C. A. DiMarzio, *Optics for Engineers* (Taylor & Francis, 2011).
54. Z. J. Coppens, W. Li, D. G. Walker, J. G. Valentine, Probing and controlling photothermal heat generation in plasmonic nanostructures. *Nano Lett.* **13**, 1023–1028 (2013).

Acknowledgments: We acknowledge T. Yuzvinsky (UCSC) for assistance with device fabrication, the W.M. Keck Center for Nanoscale Optofluidics for the use of the FEI Quanta 3D, S. Catelani (UCSC) for help with data acquisition software, and I. Hossain (UCSC) for help setting optical measurement systems and expert technical assistance. **Funding:** This work was supported by National Science Foundation grants ECCS-1611290, ECCS-1611083, ECCS-1847733, (CAREER Award), and CBET-1651385 (CAREER Award). **Author contributions:** P.Z. and A.A.Y. designed research. A.H., X.Z., M.L.M., and A.A.Y. developed the theoretical understanding and performed simulations. A.H., X.Z., U.I.C., P.Z., and A.A.Y. performed research. A.H. and A.A.Y. wrote the main parts of the manuscript. All authors suggested ways to improve the experimental validation and discussed the results. **Competing interests:** The authors declare that they have no competing interests. **Data and materials availability:** All data needed to evaluate the conclusions in the paper are present in the paper and/or the Supplementary Materials. Additional data related to this paper may be requested from the authors.

Submitted 7 November 2018
Accepted 26 September 2019
Published 18 October 2019
10.1126/sciadv.aav9786

Citation: A. Habib, X. Zhu, U. I. Can, M. L. McLanahan, P. Zorlutuna, A. A. Yanik, Electro-plasmonic nanoantenna: A nonfluorescent optical probe for ultrasensitive label-free detection of electrophysiological signals. *Sci. Adv.* **5**, eaav9786 (2019).

ScienceAdvances

Electro-plasmonic nanoantenna: A nonfluorescent optical probe for ultrasensitive label-free detection of electrophysiological signals

Ahsan Habib, Xiangchao Zhu, Uryan I. Can, Maverick L. McLanahan, Pinar Zorlutuna and Ahmet A. Yanik

Sci Adv **5** (10), eaav9786.
DOI: 10.1126/sciadv.aav9786